Supporting Information:

Ultra-rapid synthesis of the $MgCu_2$ and Mg_2Cu Laves phases and their facile conversion to nanostructured copper with controllable porosity; an energy-efficient, reversible process

Zhen Fan,[a] Gytis Baranovas,[a,b] Holly A. Yu[a], Robert Szczęsny,[c] Wei-Ren Liu[d] and Duncan H Gregory*[a]

a. WestCHEM, School of Chemistry, Joseph Black Building, University of Glasgow, Glasgow, G12 8QQ, United Kingdom.
b. Institute of Chemistry, Faculty of Chemistry and Geosciences, Vilnius University, Naugarduko str. 24, LT-03225, Vilnius, Lithuania.
c. Faculty of Chemistry, Nicolaus Copernicus University in Toruń, ul. Gagarina 7, 87-100 Toruń, Poland.
d. Department of Chemical Engineering, Chung Yuan Christian University, R&D Center for Membrane Technology, Research Center for Circular Economy, 32023, No. 200, Chun Pei Rd., Chung Li District, Taoyuan City 32023, Taiwan.
* Corresponding Author. Email: Duncan.Gregory@glasgow.ac.uk Tel: +44-141-330-8128.

Description of Supporting Information Files

1. Document

File Name: Supporting Information

Description: Documentation of supplementary experimental and analysis details.

2. Videos

File Name: Supporting Video 1

Description: MW irradiation of 60 mg of Cu powders at 200 W for 1 min under a static vacuum ($P < 10^{-6}$ mbar). The movie was played at 1X speed with a frame rate of 60 f/s.

File Name: Supporting Video 2

Description: MW synthesis of $MgCu_2$ at 200 W for 1 min under a static vacuum ($P < 10^{-6}$ mbar). The movie was played at 1X speed with a frame rate of 60 f/s.

File Name: Supporting Video 3

Description: MW synthesis of Mg_2Cu at 200 W for 1 min under a static vacuum ($P < 10^{-6}$ mbar). The movie was played at 1X speed with a frame rate of 60 f/s.

Experimental

(1) Microwave-Induced-Metal-Plasma (MIMP) Synthesis of Mg_2Cu. The MIMP method has been previously developed and reported for the synthesis of phase-pure Mg_2Sn.[1] The synthesis of Mg_2Cu was performed with the same instrument and following similar procedures. 70 mg of Mg (99.8%, 325 mesh, Alfa Aesar) and 80 mg of Cu (99.5%, 3 micron, Sigma Aldrich) powders with a molar ratio of 2.3/1 were mixed and transferred into an alumina crucible in a N_2-fed glovebox (MBraun, $O_2 < 0.5$ ppm, $H_2O < 0.5$ ppm). The crucible (7 mm in diameter and *ca*. 9 mm in height) was inserted into a quartz tube (with outer and inner diameters of 12 mm and 10 mm, respectively) and the latter closed with a fitted PTFE Young's tap in the glovebox. Both the alumina crucible and quartz tube could be viewed as MW transparent, while the small diameter of the crucible assisted in promoting the effective penetration of MWs into the powder mixture.[1] The tube was then connected to the vacuum line and placed in the cavity of a modified single-mode MW reactor (CEM, 2.45 GHz, 0 - 300 W). The quartz tube was evacuated to a pressure of $P < 10^{-6}$ mbar and closed to generate a static vacuum environment. MW irradiation was applied at 200 W for 1 min, after which the tube was naturally cooled to room temperature. The product was collected and ground in air.

(2) MIMP Synthesis of $MgCu_2$. The synthesis procedure of $MgCu_2$ was identical to Mg_2Cu with the exception that either 18 mg of Mg and 80 mg of Cu or 36 mg of Mg and 160 mg of Cu powders were used.

(3) Dealloying Experiments. HCl (ACS reagent, Sigma Aldrich) was used to prepare a 0.5 M HCl solution with deionised water. The $MgCu_2$ and Mg_2Cu powders were immersed into 200 mL of the acid (at which point gas bubbles evolved rapidly). The dealloying process generally finished in ~ 10 min for $MgCu_2$ and ~ 3 min for Mg_2Cu when no further gas bubbles appeared. Each of the powders was washed with deionised water (3 times) and ethanol (3 times), dried under vacuum for 30 min and then stored in an N_2-fed glovebox for further characterisation and measurements. The colours of the nanoporous Cu (NP-Cu) samples were pink and dark purple from $MgCu_2$ and

Mg_2Cu, respectively.

(4) Electrochemical measurements. 24 mg of NP-Cu_Mg_2Cu, 3 mg of carbon black, and 3 mg of PTFE (Polytetrafluoroethylene, Sigma Aldrich) were mixed into 5 mL of deionised water and ultrasonicated for 30 min. 10 μL of the solution was dropped on to a polished glassy carbon electrode (3 mm in diameter) and then dried overnight in a desiccator under vacuum (evacuated to ~ 1.0×10^{-1} mbar by rotary pump). The prepared electrode was used as the working electrode with Ag/AgCl and Pt electrodes used as the reference and counter electrode, respectively. A 0.1 M NaOH aqueous solution was employed as the electrolyte. The electrochemical measurements were performed with a PalmSens4 potential station.

(5) Materials Characterisation. Powder X-ray diffraction (PXD) was performed using a PANalytical X'pert Pro MPD diffractometer in Bragg−Brentano geometry (Cu−Kα1 radiation λ = 1.5406 Å; accelerating voltage of 40 kV; emission current of 40 mA). PXD patterns were collected at room temperature over a 2θ range of 15−85° with a step size of 0.0334° with scan times of 15 min (for $MgCu_2$ and Mg_2Cu) and 5 min (for NP-Cu, considering the potential air sensitivity). One PXD dataset was collected from 15-110 ° (2θ) with a step size of 0.167 ° for 1 h in order to get reliable Rietveld refinement of the phase-pure $MgCu_2$ sample. Rietveld refinement was performed through JANA 2006 software,[2] with the published $MgCu_2$ structure as an initial crystallographic model.[3] A crystallographic information file (CIF) for $MgCu_2$ was exported from JANA 2006 after the Rietveld refinement. In order to quantify the phase fractions in the high-purity Mg_2Cu sample (MW irradiation of 60 s) and so as to obtain a reasonable crystallographic model of this anti-Laves phase, Rietveld refinement was performed against PXD data using GSAS via the EXPGUI interface.[4] Suitable PXD data were collected from 15-110 °, 2θ with a step size of 0.167 ° for 2 h, with previously published Mg_2Cu and Mg structures taken as initial crystallographic models.[5,6] The Mg_2Cu/Mg two-phase refinement generated a phase fraction of 3.6(2) wt% for the Mg impurity phase. The highly asymmetric peak profile at low 2θ (< 25 °) presented some issues in fitting the peak shape with precision and led to a relatively high χ^2 value for the

refinement. A crystallographic information file (CIF) for Mg_2Cu was exported from GSAS after the refinement. The as-refined crystal structures of $MgCu_2$, Mg_2Cu and the previously published structure of Cu,[7] were plotted using the VESTA package.[8]

Scanning electron microscopy (SEM) and Energy dispersive X-ray spectroscopy (EDX) were performed using three instruments: a Hitachi S-4100 microscope equipped with an INCA X-Act detector (Oxford Instruments Analytical, UK); a Philips/FEI XL30 ESEM (beam voltage 20 kV, maximum magnification 20 k) equipped with an INCA X-Act detector (Oxford Instruments Analytical, UK) and a Carl Zeiss Sigma Variable Pressure Analytical SEM. The samples were coated with either Pt or Au plasma under vacuum to optimise the SEM image quality. Transmission electron microscopy (TEM) and selected area electron diffraction (SAED) were analysed by a TEM microscope (FEI Tecnai G2 F20 X-Twin; 200 kV, FEG) equipped with energy-dispersive X-ray spectrometer (EDAX, RTEM model SN9577; 134 eV). Measurements were performed in the TEM mode (for bright-field imaging) and in the scanning TEM (STEM) mode (for EDX). A dispersion of the sample was prepared in ethanol by ultrasonication; 5 µl of the solution was dropped onto a Ni TEM grid and stored at room temperature until the solvent had completely evaporated.

Wide survey scans (extending to the CuLM Auger region) and high resolution Cu*2p* X-ray photoelectron spectroscopy (XPS) was performed using a K-Alpha Photoelectron Spectrometer (monochromatic Al-Kα, Thermo Scientific) under vacuum. Surface-area characterisation was performed *via* N_2 adsorption-desorption isotherms measured at 77 K using a Micromeritics TriStar 3000 analyser. Surface areas of the samples were calculated and analysed from the sorption data by employing several different methods, including Brunauer – Emmett − Teller (BET) surface area, Langmuir surface area, and t-plot micropore & external surface areas based on the Harkins and Jura equation.[9] The adsorption-desorption data were further analysed using the Barrett–Joyner–Halenda (BJH) method to evaluate the distributions of pore sizes. Samples of *ca*. 150 mg were used for each adsorption-desorption measurement.

(6) Calculation of Porosity. The porosity of NPs Cu samples was calculated as below:

$$\textit{Porosity (\%)} = \frac{Cumulated\ Pore\ Volume}{Cumulated\ Pore\ Volume + Volume\ of\ Cu} * 100\% \quad \textbf{(1)}$$

The BJH adsorption cumulative volume of pores (between 1.7 – 300.0 nm in diameter) of NP-Cu_$MgCu_2$ and NP-Cu_Mg_2Cu were 0.0669 and 0.1437 $cm^3\ g^{-1}$, respectively. This volume was employed as the Cumulated Pore Volume in equation **(1)**. The volume of Cu was calculated as 1 g of Cu divided by its density. According to **Table 1** and equation **(1)**, the porosity of NP-Cu_$MgCu_2$ and NP-Cu_Mg_2Cu were 37.47% and 56.25%, respectively.

Supplementary Experiments

(1) Oxidation of NP-Cu including heating in air

In order to test the air sensitivity of NP-Cu samples, a series of experiments were performed, including the air-exposure of vacuum-dried samples; the drying of washed samples in air; chemical oxidation of the samples in liquids and finally, heating the NP-Cu samples in air to 600 ^oC at a ramp rate of 5 ^oC/min. PXD patterns in **Figure S4** confirmed that the NP-Cu samples can be very easily oxidised under the above varied conditions.

The NP-Cu samples that were heated in a furnace in air from room temperature to 600 ^oC (after which they were left to cool naturally to room temperature) were characterized in more detail. The nanoporous structure of Cu_$MgCu_2$ was fractured after heating and the appearance of the sample suggests a "layer-by-layer" volume expansion during the heating/oxidation process (**Figures S5a, b**). It appears that the outer layer of the NP-Cu_$MgCu_2$ sample is oxidised first and that the pores shrink and close, which tends to block further oxygen penetration into the inner layers of the sample. As the oxidation continues, a volume expansion leads to the cracking of the outer layer; a process that is repeated for some of the sub-surface layers. By contrast, the nanoporous structure of

NP-Cu_Mg_2Cu was maintained during aerial heating (**Figures S5c,d**), apparently due to its more open structure and its relatively wide pore-size distribution range. The EDX spectrum indicates that the experimental Cu:O atomic ratio of 51.9:48.1 is very close to the theoretical ratio of 1:1 (**Figure S5h**). The corresponding elemental mappings confirm the uniform distribution of Cu and O elements across the sample (**Figures S5e-f**). Nevertheless, the BET surface area of the CuO material oxidized from NP-Cu_Mg_2Cu is 1.524 $m^2 g^{-1}$, which is approximately an order of magnitude smaller than that of NP-Cu_Mg_2Cu (10.728 $m^2 g^{-1}$) itself. This suggests a coarsening of the Cu nano-grains (**Figures S5c**) as a result of heating and oxidation. Interestingly, the pore-size distribution however, (mainly ranging from 8-128 nm) does not differ much from that found in NP-Cu_Mg_2Cu (**Figures S5i,j**). XPS spectra provided peaks typical of *Cu2p* and *O1s* transitions for CuO (**Figures S5k,l**).

(2) MW heating of Cu starting material alone.

In order to investigate the interaction between the Cu reactant powders (99.5%, 3 micron, Sigma Aldrich) and the MW field in isolation, small samples of metal powder were heated in the MW reactor following a similar method to that described above for the syntheses of $MgCu_2$ and Mg_2Cu. In each case, 60 mg of Cu powder was placed into an alumina crucible and sealed in a quartz tube. The MW irradiation experiment was then performed at 200 W for 1 min ($P < 10^{-6}$ mbar). **Video 1** shows the pink plasma that persists throughout the MW irradiation process. As shown in **Figure S6**, Cu is found to coat a section of the quartz tube. The remainder of the Cu exists as an agglomerated powder in the alumina crucible. Evidence of some melting of Cu powder could be observed. Considering the high melting point of Cu (**Figure S1**) and the formation of Cu plasma, the experimental results suggest that the Cu powder couples very effectively with the MW field (as one might expect for a highly conducting, finely divided, metal powder).

(3) MW reaction of NP Cu with Mg

In order to investigate the potential reverse reaction between NP Cu and Mg powders and so as to illustrate that the entire synthetic process could be cycled, a synthesis experiment was performed using a powder mixture of NP Cu_$MgCu_2$ (80 mg) and Mg (18 mg) at 200 W for 60 s under a pressure of $P < 10^{-6}$ mbar. PXD patterns (**Figure S7**) confirmed that pure $MgCu_2$ alloy was formed, proving that our process is not only energy-efficient but also reversible, *i.e.,* demonstrating that the Cu products could be (re)cycled multiple times.

Figures and Tables

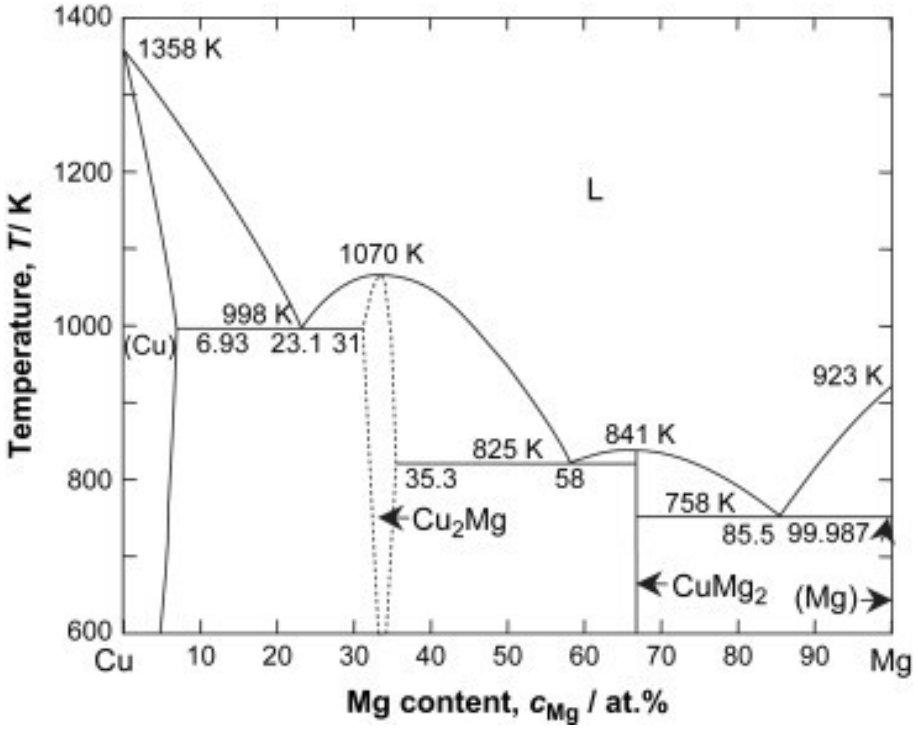

Figure S1. The phase diagram of Mg – Cu binary system. Adapted from [10].

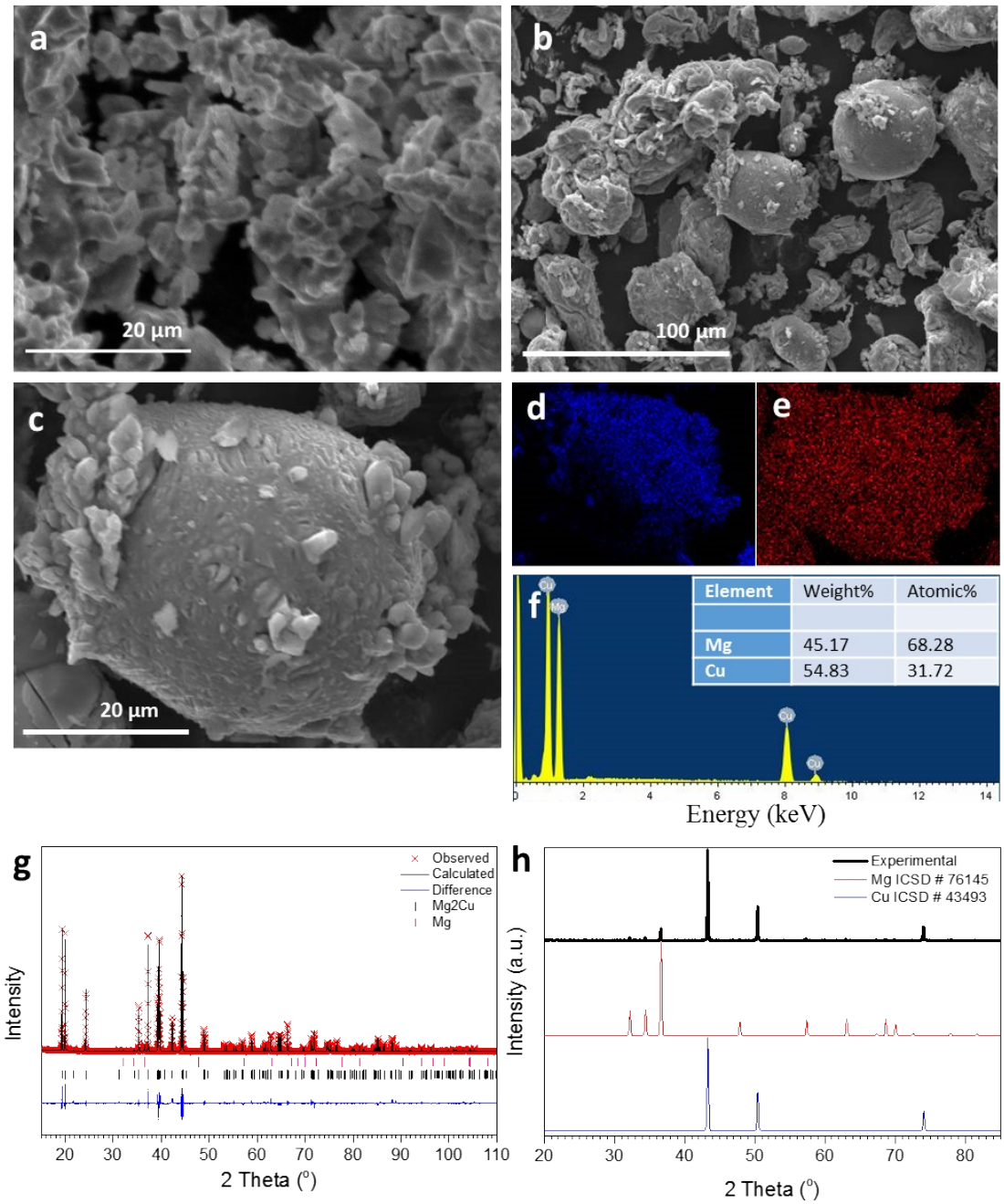

Figure S2. **(a)** SEM image of an as-synthesised, phase-pure sample of $MgCu_2$ powder; **(b, c)** SEM images of an as-synthesised Mg_2Cu sample taken at different magnifications; **(d, e)** EDX elemental mapping of Mg (blue) and Cu (red) of the sample area shown in (c); **(f)** the corresponding EDX spectrum taken from an area scan across the sample shown in (c); **(g)** Rietveld profile plot for Mg_2Cu synthesised by MW irradiation for 60 s; and **(h)** PXD pattern of the powder product (black) following the 1:2 Mg:Cu synthesis performed for 30 s - standard patterns of Mg (red) and Cu (blue) are shown for comparison.

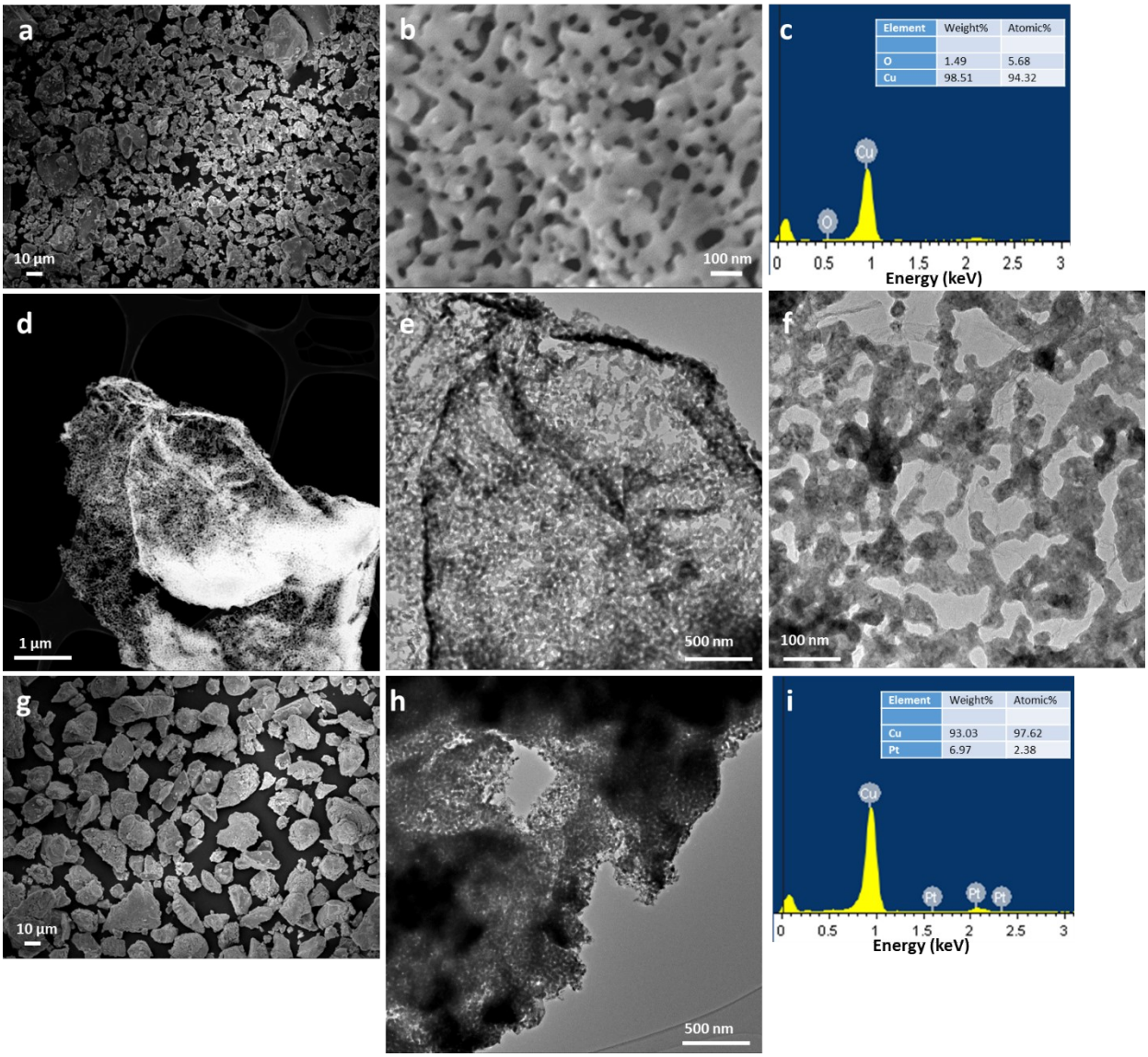

Figure S3. (a, b) Low and higher magnification SEM images of NP-Cu_$MgCu_2$; **(c)** EDX spectrum of NP-Cu_$MgCu_2$ taken from the area shown in ***Figure 2a*** in the main article; **(d)** Low-resolution STEM image of NP-Cu_$MgCu_2$; (**e, f**) Low-resolution TEM images of NP-Cu_$MgCu_2$; **(g)** Low magnification SEM image of NP-Cu_Mg_2Cu; **(h)** Low-resolution TEM image of NP-Cu_Mg_2Cu and **(i)** EDX spectrum of NP-Cu_Mg_2Cu taken from the area shown in ***Figure 4b*** in the main article.

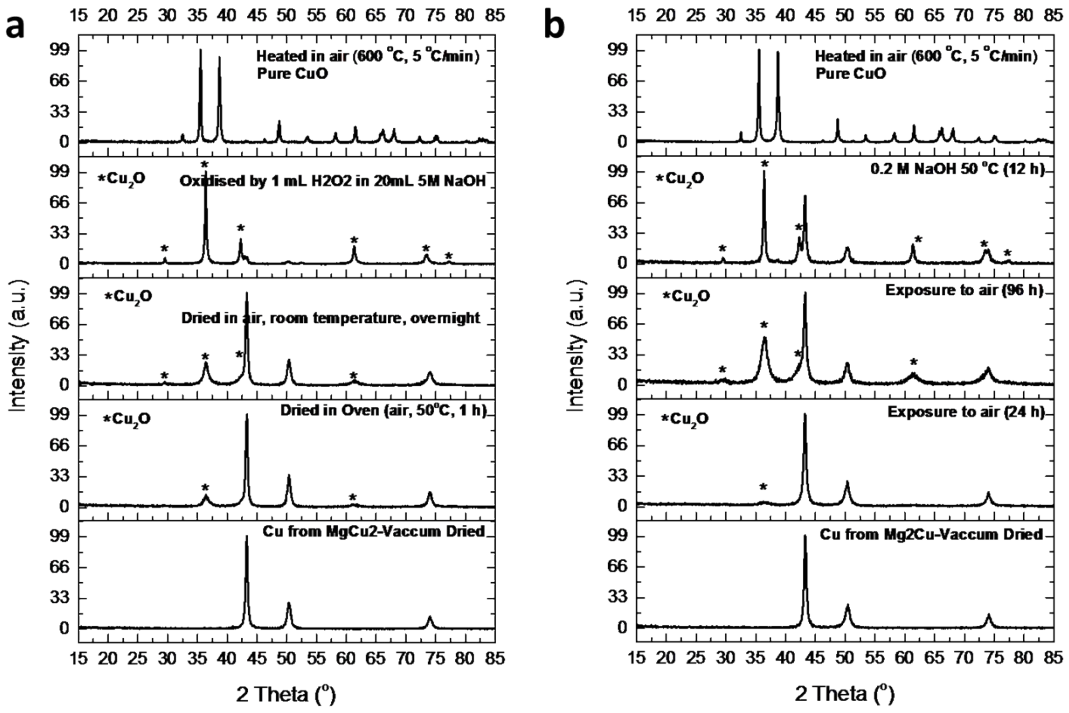

Figure S4. PXD patterns taken after the oxidation of the NP-Cu samples. The method of oxidation is annotated on each part of the figure: **(a)** NP-Cu_$MgCu_2$ and **(b)** NP-Cu_Mg_2Cu.

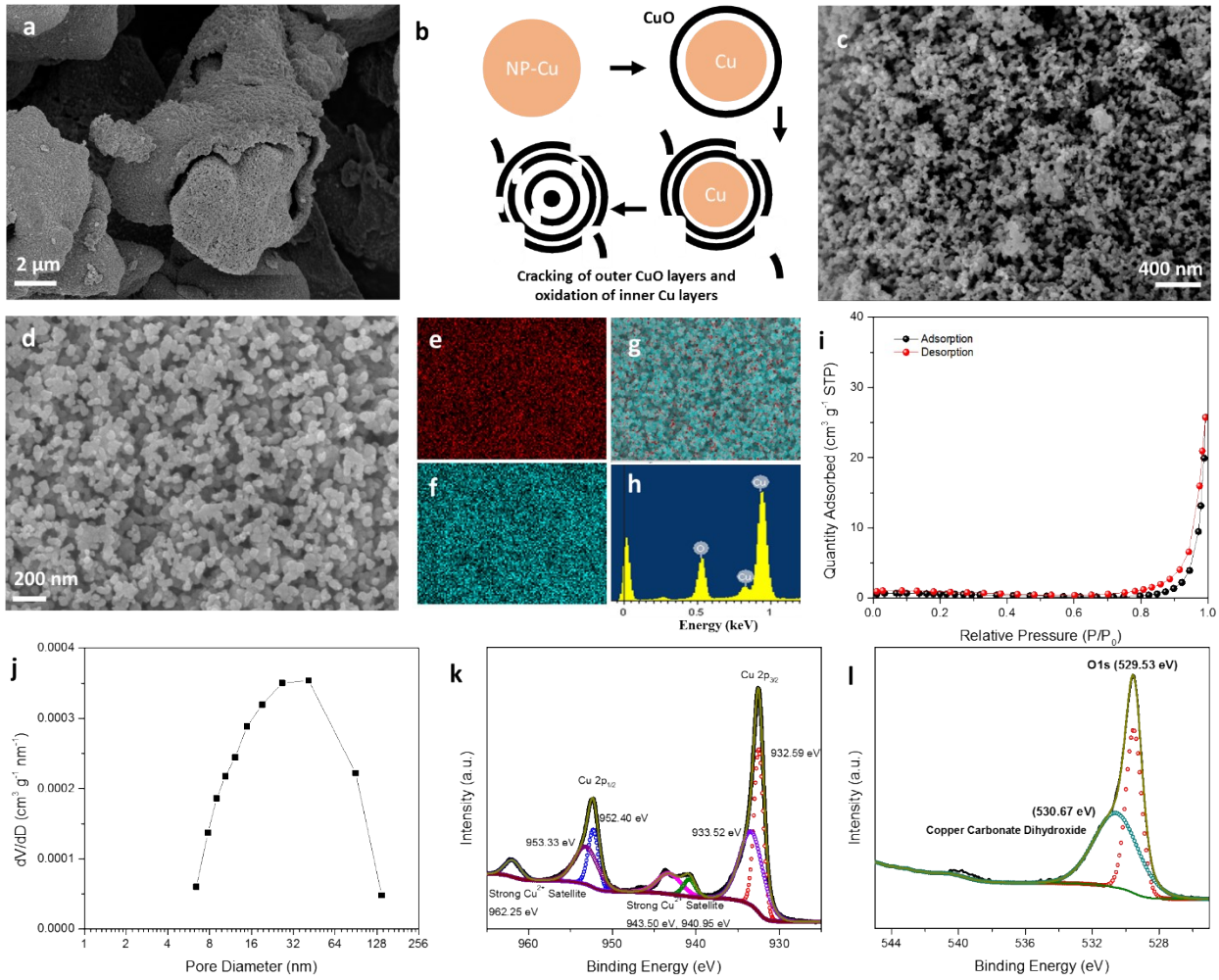

Figure S5. (a) SEM image of single phase CuO produced by heating NP-Cu_$MgCu_2$ to 600 °C in air; **(b)** schematic of the possible layer-by-layer oxidation and volume expansion during the heating of NP-Cu_$MgCu_2$ at 600 °C in air based on the structures seen in the image in (a); **(c, d)** SEM images of single-phase CuO prepared by heating NP-Cu_Mg_2Cu to 600 °C in air; **(e-h)** elemental maps from EDX for O (e), Cu (f) and both Cu and O (g) and the corresponding EDX spectrum (h) taken across the area of the image shown in (d); **(i, j)** BET N_2 physisorption isotherms and pore-size distributions of single phase CuO prepared by heating NP-Cu_Mg_2Cu to 600 °C in air; and **(k, l)** Cu*2p* and O*1s* XPS spectra of single phase CuO prepared by heating NP-Cu_Mg_2Cu to 600 °C in air.

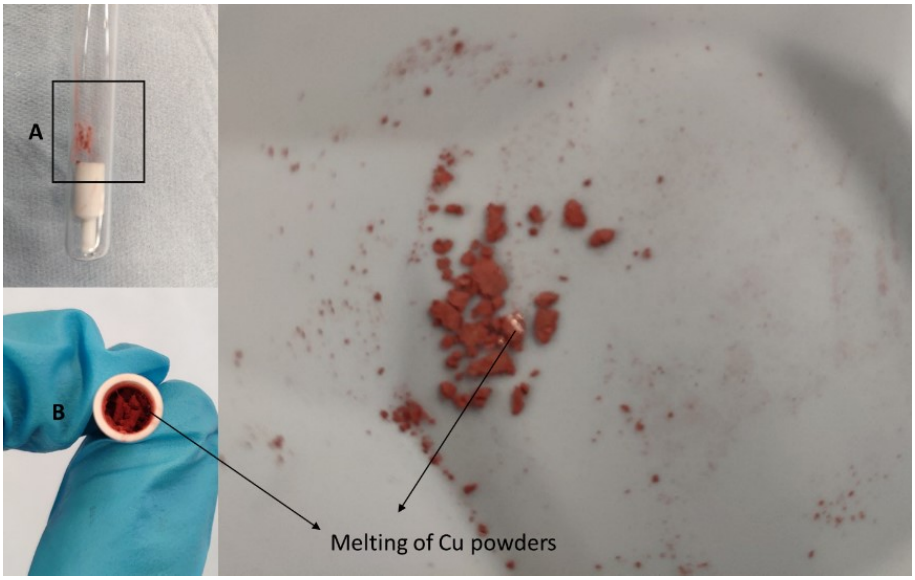

Figure S6. Images of the quartz tube with a section of it coated with Cu (A) and inner alumina reaction crucible (B) after the MW irradiation of Cu powder (alone) at 200 W for 1 min under a static vacuum ($P < 10^{-6}$ mbar).

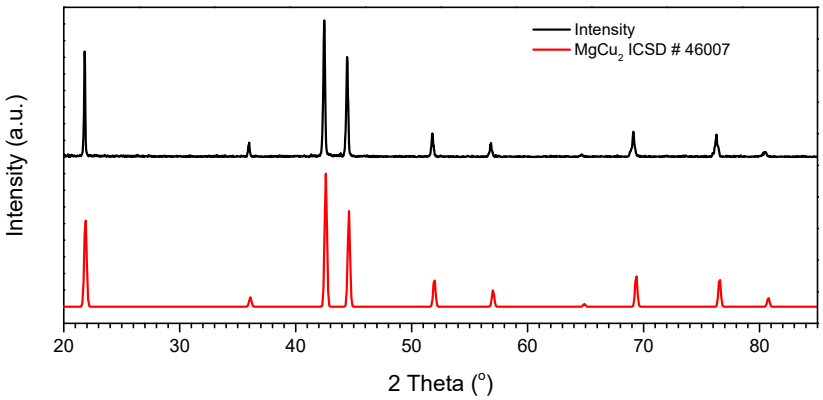

Figure S7. PXD pattern of $MgCu_2$ synthesised from a mixture of Mg powder and NP-Cu_$MgCu_2$ at 200 W for 60 s (black) as compared to a standard pattern for $MgCu_2$ (red).

Table S1. Synthesis procedures and parameters of the parent alloys for NP Cu in some reported studies.

References in main manuscript	Parent alloys	Alloy preparation method	Atmosphere
4. K. Nishimoto *et al.*, *Inorg. Chem.*, 2018, 57, 2908-2916.	Al_2Cu	(1) Arc melting of Al-Cu (2) Annealing of Al_2Cu at 823 K / 24 h	Ar
6. X. Zhang *et al.*, *Chem. Comm.*, 2018, 54, 5446-5449.	CuCa, & $CuCa_2$	High frequency induction heating of Ca-Cu (ramped to 873 K in 2 min)	Not known
24. H. Xu, *et al.*, *Nano Res.*, 2016, 9, 2467-2477.	$Mg_{65}Cu_{25-x}(Pt,Au)_xY_{10}$	(1) Arc melting of Cu-Y (2) Arc melting of Cu-Y-Mg (3) High frequency induction heating (4) Melt-spinning of $Mg_{65}Cu_{25-x}(Pt, Au)_xY_{10}$	Ar
34. C. Zhao *et al.*, *Corros. Sci.*, 2009, 51, 2120-2125.	"$Mg_{67}Cu_{33}$", "$Mg_{60}Cu_{40}$", "$Mg_{50}Cu_{50}$", "$Mg_{40}Cu_{60}$" & "$Mg_{33}Cu_{67}$"	(1) Resistance furnace melting of Mg-Cu (2) Melt casting with iron-chill mould (3) High frequency induction heated melt-spinning.	Ar
35. D. Liu *et al.*, *Nanoscale*, 2013, 5, 1917-1921.	$Al_{50}Cu_{50}$	Electron-beam melting of Al-Cu (No further information provided)	Not known
This Study	$MgCu_2$ & Mg_2Cu	Microwave-Induced-Metal-Plasma (MIMP) synthesis; 1 min / 200 W [a]	Vacuum

[a] Ultra-fast MIMP reactions with no melting observed for the synthesised $MgCu_2$ and Mg_2Cu products. Both products are fine powders, which need no further processing.

Table S2. Crystallographic data for MW-synthesised $MgCu_2$ from the Rietveld refinement against PXD data.

Chemical Formula	$MgCu_2$
Crystal System	Cubic
Space Group	*Fd*-3*m* (227)
Lattice Parameter, a / Å	7.0439(1) (*vs.* 7.034(2)) [a]
Formula Weight / g mol^{-1}	1172.88
Formula Units, Z	8
Calculated Density / g cm^{-3}	5.5727 (*vs.* 5.78) [a]
No. of Observations	5686
No. of Parameters	30
χ^2	2.789
Rp	0.0725
wRp	0.1113

[a] From the previously published structure of $MgCu_2$.[3]

Table S3. Atomic parameters of $MgCu_2$ from the Rietveld refinement against PXD data.

Atom	Wyckoff Symbol	x	y	z	$100 \times U_{iso}$ / Å^2 (Equivalent)	Thermal Displacement Parameters, U_{ij} / Å^2	Occupancy
Mg	8*a*	0.125	0.125	0.125	1.16(4)	$U^{11}=U^{22}=U^{33}=0.0116(6)$ $U^{12}=U^{13}=U^{23}=0$	1.00
Cu	16*d*	0.5	0.5	0.5	0.76(1)	$U^{11}=U^{22}=U^{33}=0.0076(2)$ $U^{12}=U^{13}=U^{23}=-0.0018(2)$	0.962(4) (*vs.* 1)[a]

[a] From the previously published structure of $MgCu_2$.[3]

Table S4. Selected interatomic distances in the structure of $MgCu_2$ from the Rietveld Refinement against PXD data.

Atoms	Distance / Å
Cu-Cu	2.49041(3) (*vs.* 2.4869(5))[a]
Cu-Mg	2.92026(5) (*vs.* 2.9161(7))[a]
Mg-Mg	3.05012(3) (*vs.* 3.0458(5))[a]

[a] From the previously published structure of $MgCu_2$.[3]

Table S5. Crystallographic data for MW-synthesised Mg_2Cu from the Rietveld refinement against PXD data.

Chemical Formula	Mg_2Cu	Mg
Crystal System	Orthorhombic	hexagonal
Space Group	*FdddZ* (70)	*P63/mmc* (194)
Lattice Parameter / Å	5.28212(8)	3.2103(4)
	9.0600(2)	3.2103(4)
	18.3475(3)	5.2132(10)
Formula Weight / g mol^{-1}	1746.144	48.610
Formula Units, Z	16	2
Calculated Density / g cm^{-3}	3.302	1.735
Phase Fraction (%)	94.4(2)	3.6(2)
No. of Observations	5685	
No. of Parameters	76	
χ^2	6.969	
Rp	0.1255	
wRp	0.1646	

Table S6. Atomic parameters of Mg_2Cu from the Rietveld refinement against PXD data.

Atom	Wyckoff Symbol	x	y	z	Thermal Displacement Parameters, U_{ij} / Å²	Occupancy
Mg	16g	0.125	0.125	0.0413(1)	U^{11}=0.026(2) U^{12}=-0.006(2) U^{13}=0 U^{22}=0.050(3) U^{23}=0 U^{33}=0.014(2)	1.00
Mg	16f	0.125	0.4578(3)	0.125	U^{11}=0.018(2) U^{12}=0 U^{13}=-0.004(2) U^{22}=0.027(2) U^{23}=0 U^{33}=0.009(2)	1.00
Cu	16g	0.125	0.125	0.49819(6)	U^{11}=0.023(1) U^{12}=-0.005(1) U^{13}=0 U^{22}=0.029(1) U^{23}=0 U^{33}=0.006(1)	0.952(6)

Table S7. Selected interatomic distances and angles in the structure of Mg_2Cu from the Rietveld Refinement against PXD data.

Distance / Å	Angle / °
Cu-Cu: 2.6227(1)	Cu-Cu-Cu: 176.73(11)
Cu-Mg: 2.7572(9), 2.7231(12)	Cu-Mg-Cu: 57.16(6), 56.95(6)
Mg-Mg: 3.0291(19), 3.4097(17), 3.029(4)	Mg-Cu-Mg: 122.79(10), 77.57(8), 123.04(7)

Table S8_1 Indexed Lattice Planes from the SAED Pattern shown in *Figure 2f*

Diffraction No.	Indexed Diffraction Distance / nm	Phase; Lattice Plane
1	0.300	Cu_2O; (011)
2	0.245	Cu; (110)
		Cu_2O; (111)
3	0.212	Cu; (111)
		Cu_2O; (002)
4	0.179	Cu; (200)
5	0.150	Cu_2O; (220)
6	0.127	Cu; (220)
7	0.111	Cu; (311)
8	0.105	Cu; (222)

Table S8_2 Indexed Lattice Planes from the SAED Pattern shown in *Figure 3b*

Diffraction No.	Indexed Diffraction Distance / nm	Phase; Lattice Plane
1	0.300	Cu_2O; (011)
2	0.245	Cu; (110)
		Cu_2O; (111)
3	0.209	Cu; (111)
		Cu_2O; (002)
4	0.175	Cu; (200)
5	0.150	Cu_2O; (220)
6	0.128	Cu; (220)
7	0.110	Cu; (311)
8	0.105	Cu; (222)
9	0.082	Cu; (133)

Table S8_3 Indexed Lattice Planes from the SAED Pattern shown in *Figure 4f*

Diffraction No.	Indexed Diffraction Distance / nm	Phase; Lattice Plane
1	0.302	Cu_2O; (011)
2	0.246	Cu; (110)
		Cu_2O; (111)
3	0.208	Cu; (111)
		Cu_2O; (002)
4	0.180	Cu; (200)
5	0.152	Cu_2O; (220)
6	0.128	Cu; (220)
7	0.109	Cu; (311)
8	0.083	Cu; (133)

Table S9. Non-enzymatic glucose linear-sensing ranges and sensitivities for selected Cu-based nanomaterials.

Electrode	Linear Sensing Range / mM	Sensitivity / $\mu A\ mM^{-1}\ cm^{-2}$	Correlation Coefficient R	Potential	Reference
CuO Nanoribbons	0.05-3.5	412	0.9950	+0.40 V *vs.* Ag/AgCl	11
Nanoporous Cu	0.01-0.5	220	0.998	+0.45 V *vs.* Ag/AgCl	12
	0.5-10	60	0.997		
Cu-Cu_2O Nanoporous Nanoparticle	0.01-5.5	123.8	0.9986	+0.60 V *vs.* Ag/AgCl	13
Nanoporous Cu	0.5-5	22.4	0.9997	+0.50 V *vs.* SCE[b]	14
	5-22	19.2	0.9995		
Nanoporous Pd-Cu	0.5-20	-	0.9970	+0.80 V *vs.* RHE[c]	15
CuO Nanosheet / CC[a]	0.001-1.0	4902	-	+0.55 V *vs.* Ag/AgCl	16
CuO Nanowires / CC	0.001-1.12	2973.2	-		
CuO Nanoparticle / CC	0.001-1.22	1245.9	-		
Nanoporous Cu_Mg_2Cu	0.5-4.5	573.3	0.9963	+0.62 V *vs.* Ag/AgCl	**This Work**
	4.5-10.0	349.7	0.9961		
Nanoporous Cu_$MgCu_2$	0.5-4.5	498.5	0.9995		
	4.5-10.0	411.0	0.9998		

[a] CC: Carbon cloth; [b] SCE: Saturated Calomel Electrode; [c] RHE: Reversible Hydrogen Electrode.

References

[1] Z. Fan, M.D. Cappelluti, and D.H. Gregory, ACS Sustainable Chemistry & Engineering, 2019, **7**(24), 19686-19698.

[2] V. Petricek, M. Dusek, L. Palatinus, Zeitschrift für Kristallographie-Crystalline Materials, 2014, **229**(5), 345-352.

[3] T. Ohba, Y. Kitano, and Y. Komura, Acta Crystallographica Section C: Crystal Structure Communications, 1984, **40**(1), 1-5.

[4] B.H. Toby, Journal of Applied Crystallography, 2001, **34**(2), 210-213.

[5] M.H. Braga, J.J.A. Ferreira, and J. Siewenie *et al*., Journal of Solid State Chemistry, 2010, **183**(1), 10-19.

[6] H.E. Swanson, T. Eleanor, K.F. Ruth, National Bureau of Standards Circular (U. S.). 1953, **539**, 1-95.

[7] H.M. Otte, Journal of Applied Physics, 1961, **32**(8), 1536-1546.

[8] K. Momma, and F. Izumi, Journal of Applied Crystallography, 2011, **44**(6), 1272-1276.

[9] S. Shanavas, A.S. Kunju, H.T.Varghese, and C.Y. Panicker, Oriental J. Chemistry, 2011, **27**(1), 245.

[10] A. Takeuchi, K. Yubuta, and A. Inoue, Intermetallics, 2008, **16**(11-12), 1273-1278.

[11] R.K. Sahoo, A. Das, and K. Samantaray *et al.*, CrystEngComm, 2019, **21**(10), 1607-1616.

[12] S. Sattayasamitsathit, P. Thavarungkul, and C.Thammakhet *et al.*, Electroanalysis, 2009, **21**(21), 2371-2377.

[13] Y.X. Zhao, Y.P. Li, and Z.Y. He *et al.*, RSC Advances, 2013, **3**(7), 2178-2181.

[14] H. Xu, S. Pang, and Y. Jin *et al.*, Nano Research, 2016, **9**(8), 2467-2477.

[15] A.H. Liu, H.R. Geng, and C.X. Xu *et al.*, Analytica Chimica Acta, 2011, **703**(2), 172-178.

[16] Y. Zhang, T. Shi, and Z. Liu *et al.*, Sensors and Actuators B: Chemical, 2016, **236**, 326-333.